

Modeling dynamical ejecta from binary neutron star mergers and implications for electromagnetic counterparts

Tim Dietrich¹, Maximiliano Ujevic²

¹ Max Planck Institute for Gravitational Physics, Albert Einstein Institute, D-14476 Golm, Germany

²Centro de Ciências Naturais e Humanas, Universidade Federal do ABC, 09210-580, Santo André, São Paulo, Brazil

Abstract. In addition to the emission of gravitational waves (GWs) the coalescence and merger of two neutron stars will produce a variety of electromagnetic (EM) signals. In this work we combine a large set of numerical relativity simulations performed by different groups and we present fits for the mass, kinetic energy, and the velocities of the dynamical ejected material. Additionally, we comment on the geometry and composition of the ejecta and discuss the influence of the stars' individual rotation.

The derived fits can be used to approximate the luminosity and lightcurve of the kilonovae (macronovae) and to estimate the main properties of the radio flares. This correlation between the binary parameters and the EM signals allows in case of a GW detection to approximate possible EM counterparts when first estimates of the masses are available. After a possible kilonovae observation our results could also be used to restrict the region of the parameter space which has to be covered by numerical relativity simulations.

PACS numbers: 04.25.D-, 04.30.Db, 95.30.Sf, 95.30.Lz, 97.60.Jd

1. Introduction

The first detections of coalescing binary black hole (BBH) systems [1, 2] inaugurated the field of gravitational wave (GW) astronomy. Beside BBHs, binary neutron stars (BNS) are one of the expected sources for future GW detections [3, 4]. In contrast to BBH mergers, it is expected that BNS mergers produce electromagnetic (EM) signals, as kilonovae (also called macronovae), radio flares or short gamma-ray bursts (SGRBs). While SGRBs are powered by collimated highly relativistic outflows, e.g., [5, 6, 7], kilonovae are transient emissions in the optical or near-infrared band, e.g., [8, 9, 10], produced by the radioactive decay of r-process nuclei in the neutron-rich material ejected during the merger. Additionally, mildly and sub-relativistic outflows can generate synchrotron radiation (radio flares) even years after the merger of the two neutron stars, see e.g., [11].

One possibility to study BNS mergers are numerical relativity (NR) simulations. Those simulations allow to describe the system even beyond the merger of the two stars solving Einsteins field equations. Over the last years more microphysical descriptions have been included, e.g., realistic equation of states (EOSs), neutrino transport, magnetic fields. It also has become a common approach to extract information from NR simulations about the unbound material ejected from the system and use these information to estimate possible EM counterparts. However, the computation of ejecta and lightcurves is still challenging. While current state-of-the art numerical simulations cover the last 10 – 20 orbits before and up to ~ 50 ms after the merger, it is computationally too expensive to study the dynamical ejected material longer than a fraction of a second. But, it is possible to use relativistic simulations as initial conditions and either assume free expansion of the ejecta material, e.g., [12], evolution on a fixed spacetime background, e.g., [13, 14], or use radiative transfer Monte-Carlo simulations, e.g., [15, 16]. Our work is complementary to most previous studies, we will use a large set of numerical relativity data obtained from different groups to derive phenomenological fits relating the binary parameters to the ejecta properties. Knowing the basic properties of the ejecta allows to give estimates on the expected kilonovae and radio flares.

In general, the time between a GW detection and the observation of the corresponding kilonovae (about a few days) is not long enough to perform full NR simulations which have typical run times of weeks to months. Therefore, NR simulations can only be used for comparison once GW and EM observations finish. The advantage of the phenomenological model proposed in this article is that even before the EM follow up observations start first estimates of the kilonovae properties can be given. Furthermore, after the kilonovae has been detected, the model can be used to reduce the part of the BNS parameter space which has to be covered by full NR simulations.

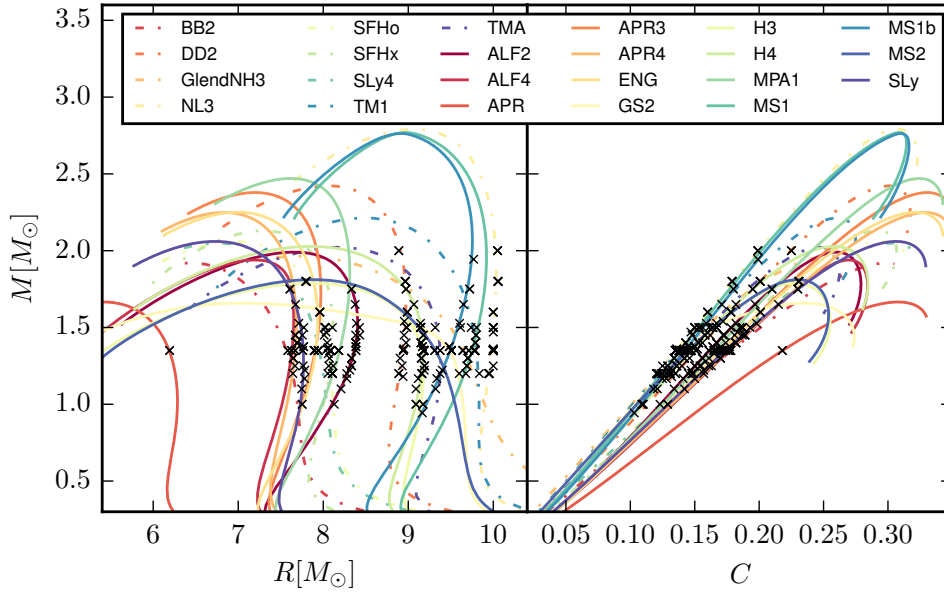


Figure 1. Mass vs. radius relations (left) and mass vs. compactness relations (right) for all EOSs used in this work. Tabulated EOSs are marked with dashed lines, piecewise polytropes with solid lines. The markers refer to configurations employed in this work.

2. Employed Dataset

Over the last years numerical relativity (NR) has made a tremendous progress and a large number of groups have studied the merger process of BNSs, see e.g., [17, 18] and references therein. Despite the computation of the emitted GW signal, the investigation of ejected material and EM counterparts went into the focus of research.

Combining published work from different groups enables us to obtain an NR catalog to derive fitting formulas for important ejecta quantities. In this article we use results from [19, 20, 21, 22, 23, 24], where the mass, kinetic energy, and velocity of the ejecta are reported. The data set combines results based on grid structured codes [19, 21, 22, 23, 24] with results employing a SPH code [20] under conformal flatness approximation and it includes simplifies EOSs, tabulated EOS as well as simulations with and without neutrino treatment. In total 172 simulations have been considered.

Although simulation techniques are continuously improved and higher accuracy is achieved, the characterization of ejecta is still challenging and results have to be assigned with large uncertainties. Considering the accuracy of the NR data points, quantities as the mass and kinetic energy have uncertainties which range between $\sim 10\%$ up to even $\sim 100\%$, see e.g., appendix A of [19] and table III of [24], where multiple resolutions have been employed. In general one finds that the fractional uncertainty is larger for lower massive ejecta.

In addition to the uncertainty of the results employing the same numerical code also differences between different implementations/codes exist. For some cases those discrepancies are quite large (up to a factor of ~ 5 in extreme cases) and they also

depend on the implementation of thermal effects and if neutrino cooling or transport is included in the simulations. Those differences can produce systematic uncertainties. We try to minimize selection effects by including a large number of simulations produced by a variety of numerical codes. In the future crosschecks among different codes employing the same physical systems will be needed for a better estimate of systematic errors.

In our work, we restrict our analysis to dynamical ejecta. Ejecta produced after BH formation are not included, but will contribute to the total amount of ejecta and to the corresponding EM signals, see e.g., [25]. Thus, our results can be seen as lower bounds for the luminosity of EM observables. Furthermore, while some of our data points were computed by NR simulations including neutrinos and tabulated EOSs, the effect of magnetic fields is not studied, although magnetic fields will influence the binary dynamics shortly around and after merger and lead to mass ejection by magnetic winds.

The complete dataset is reported in table 1, where a simulation number is assigned to every data point (first column). In total we consider 23 different EOSs (shown in figure 1). Most EOSs are represented by a piecewise polytrope fitted to a zero-temperature EOS (straight lines), see e.g., [26]. An additional thermal contribution to the pressure according to $p_{\text{th}} = \rho\epsilon(\Gamma_{\text{th}} - 1)$ is added for the evolution, where ρ is the rest-mass density and ϵ the internal energy. The parameter Γ_{th} is also reported in table 1. Some simulations use full tabulated EOSs (dashed lines), which we denote as full in table 1. Simulations with tabulated EOSs and neutrino treatment are denoted with fullN. In addition to the parameters describing the binary, we report the mass of the ejected material M_{ej} , the kinetic energy T_{ej} , the average velocity inside the orbital plane v_{ρ} , the average velocity perpendicular to the orbital plane v_z , and the total velocity v_{ej} .

Table 1: NR data used in this work. Columns refer to: The data ID, cf. e.g., figure 2, mass of the first star M_1 , mass of the second star M_2 , Γ_{th} modeling thermal effects for piecewise polytropic EOS, ejecta mass M_{ej} , kinetic energy of the ejecta T_{ej} , average velocity inside the orbital plane v_{ρ} , average velocity perpendicular to the orbital plane v_z , total average ejecta velocity v_{ej} . In cases where v_{ρ} and v_z are given, we estimate the total ejecta velocity as $v_{\text{ej}} = \sqrt{v_{\rho}^2 + v_z^2}$. Note that in [23] the ejecta velocity was estimated based on $T_{\text{ej}} = M_{\text{ej}}v_{\text{ej}}^2/2$, consequently we use this relation to compute the kinetic energy not stated in [23].

#	Ref	EOS	M_1 [M_{\odot}]	M_2 [M_{\odot}]	Γ_{th}	M_{ej} [$10^{-3}M_{\odot}$]	T_{ej} [10^{50}erg]	v_{ρ} [c]	v_z [c]	v_{ej} [c]
1	ALF2	[24]	1	1.75	1.75	36	12.69	0.18	0.03	0.18
2	ALF2	[24]	1.167	1.75	1.75	25	10.73	0.19	0.06	0.2
3	ALF2	[24]	1.1	1.65	1.75	24	7.5	0.17	0.07	0.18
4	ALF2	[24]	1	1.5	1.75	21	4.8	0.15	0.07	0.17
5	ALF2	[24]	1.222	1.527	1.75	7.5	3.93	0.17	0.12	0.21
6	ALF2	[19]	1.2	1.5	1.8	5.5	3	0.21	0.1	0.23
7	ALF2	[19]	1.25	1.45	1.8	3	1.5	0.2	0.1	0.22
8	ALF2	[19]	1.3	1.4	1.8	1.5	0.8	0.16	0.11	0.19

9	ALF2	[19]	1.4	1.4	1.8	2.5	1.5	0.21	0.13	0.25
10	ALF2	[24]	1.375	1.375	1.75	3.4	1.36	0.17	0.1	0.2
11	ALF2	[19]	1.35	1.35	1.8	2.5	1.5	0.22	0.12	0.25
12	ALF2	[19]	1.3	1.3	1.8	2	1	0.19	0.1	0.21
13	APR4	[19]	1.2	1.5	2	7.5	5.5	0.24	0.12	0.27
14	APR4	[19]	1.2	1.5	1.8	8	5.5	0.23	0.11	0.25
15	APR4	[19]	1.2	1.5	1.6	9	5	0.2	0.1	0.22
16	APR4	[19]	1.3	1.6	1.8	2	1.5	0.24	0.08	0.25
17	APR4	[19]	1.2	1.4	1.8	3	2	0.21	0.12	0.24
18	APR4	[19]	1.25	1.45	1.8	7	4.5	0.22	0.11	0.25
19	APR4	[19]	1.3	1.5	1.8	12	8.5	0.23	0.12	0.26
20	APR4	[19]	1.3	1.4	1.8	8	5	0.19	0.12	0.22
21	APR4	[19]	1.25	1.35	1.8	5	3	0.18	0.1	0.21
22	APR4	[19]	1.4	1.5	1.8	0.6	0.9	0.35	0.12	0.37
23	APR4	[19]	1.45	1.45	1.8	0.1	0.1	0.29	0.13	0.32
24	APR4	[19]	1.4	1.4	1.8	14	10	0.22	0.15	0.27
25	APR4	[19]	1.35	1.35	2	5	3	0.19	0.13	0.23
26	APR4	[19]	1.35	1.35	1.8	7	4	0.19	0.12	0.22
27	APR4	[19]	1.35	1.35	1.6	11	6	0.19	0.13	0.23
28	APR4	[19]	1.3	1.3	1.8	2	1	0.19	0.1	0.21
29	H4	[24]	1	1.75	1.75	40	12.51	0.17	0.02	0.17
30	H4	[24]	1.167	1.75	1.75	14	4.65	0.18	0.05	0.19
31	H4	[24]	1.1	1.65	1.75	17	4.83	0.17	0.04	0.17
32	H4	[24]	1	1.5	1.75	27	8.04	0.17	0.03	0.17
33	H4	[24]	1.222	1.527	1.75	6.6	3.04	0.18	0.11	0.21
34	H4	[19]	1.2	1.5	2	4	2	0.21	0.09	0.23
35	H4	[19]	1.2	1.5	1.8	3.5	2	0.21	0.09	0.23
36	H4	[19]	1.2	1.5	1.6	4.5	2	0.19	0.1	0.21
37	H4	[19]	1.2	1.4	1.8	2.5	1	0.19	0.1	0.21
38	H4	[19]	1.25	1.45	1.8	2	1.5	0.19	0.1	0.21
39	H4	[19]	1.3	1.5	1.8	3	2	0.19	0.1	0.21
40	H4	[19]	1.3	1.4	1.8	0.7	0.4	0.18	0.1	0.21
41	H4	[19]	1.25	1.35	1.8	0.6	0.3	0.18	0.1	0.21
42	H4	[19]	1.4	1.4	1.8	0.3	0.2	0.17	0.13	0.21
43	H4	[24]	1.375	1.375	1.75	3.4	1.59	0.19	0.1	0.21
44	H4	[19]	1.35	1.35	2	0.4	0.2	0.2	0.1	0.22
45	H4	[19]	1.35	1.35	1.8	0.5	0.2	0.19	0.11	0.22
46	H4	[19]	1.35	1.35	1.6	0.7	0.4	0.21	0.11	0.24
47	H4	[19]	1.3	1.3	1.8	0.3	0.1	0.16	0.1	0.19
48	MS1	[19]	1.2	1.5	1.8	3.5	1.5	0.19	0.1	0.21
49	MS1	[19]	1.25	1.45	1.8	1.5	0.8	0.19	0.11	0.22
50	MS1	[19]	1.3	1.4	1.8	0.6	0.2	0.17	0.09	0.19
51	MS1	[19]	1.4	1.4	1.8	0.6	0.2	0.13	0.09	0.16
52	MS1	[19]	1.35	1.35	1.8	1.5	0.6	0.14	0.08	0.16
53	MS1	[19]	1.3	1.3	1.8	1.5	0.5	0.15	0.08	0.17
54	MS1b	[24]	0.944	1.944	1.75	65	21.45	0.18	0.02	0.18
55	MS1b	[24]	1	1.75	1.75	49	15.19	0.17	0.03	0.17
56	MS1b	[24]	1.167	1.75	1.75	24	7.69	0.18	0.05	0.19
57	MS1b	[24]	1.1	1.65	1.75	26	7.33	0.17	0.04	0.17
58	MS1b	[24]	1	1.5	1.75	32	7.87	0.16	0.03	0.16
59	MS1b	[24]	1.222	1.527	1.75	4.8	1.64	0.15	0.11	0.19
60	MS1b	[24]	1.375	1.375	1.75	2.3	0.39	0.13	0.06	0.14
61	SLy	[24]	1	1.75	1.75	24	8.94	0.19	0.03	0.19

62	SLy	[24]	1.167	1.75	1.75	6.5	5.54	0.25	0.11	0.27
63	SLy	[24]	1.1	1.65	1.75	16	7.69	0.19	0.11	0.22
64	SLy	[24]	1	1.5	1.75	18	9.12	0.19	0.12	0.22
65	SLy	[24]	1.222	1.527	1.75	18	8.4	0.16	0.11	0.19
66	SLy	[24]	1.375	1.375	1.75	16	4.83	0.17	0.1	0.2
67	ALF2	[21]	1.25	1.45	1.75	3.9	0.8	-	-	0.15
68	ALF2	[20]	1.35	1.35	2	3.8	3.36	-	-	0.28
69	ALF2	[21]	1.35	1.35	1.75	3.5	0.7	-	-	0.15
70	ALF2	[20]	1.35	1.35	1.5	4.49	3.8	-	-	0.27
71	ALF4	[20]	1.35	1.35	2	5.7	6.07	-	-	0.3
72	ALF4	[20]	1.35	1.35	1.5	7.4	7.65	-	-	0.29
73	APR	[20]	1.35	1.35	2	5.96	6.37	-	-	0.31
74	APR	[20]	1.35	1.35	1.5	7.38	7.9	-	-	0.3
75	APR3	[20]	1.35	1.35	2	4.65	4.69	-	-	0.3
76	APR3	[20]	1.35	1.35	1.5	6.15	5.5	-	-	0.27
77	DD2	[20]	1.2	1.8	full	17.08	6.72	-	-	0.17
78	DD2	[20]	1.35	2	full	6.41	9.64	-	-	0.31
79	DD2	[20]	1.35	1.8	full	14.85	9.48	-	-	0.21
80	DD2	[20]	1.2	1.6	full	10.9	6.39	-	-	0.2
81	DD2	[22]	1.18	1.54	fullN	1.3	0.76	-	-	0.3
82	DD2	[20]	1.2	1.5	full	8.79	4.97	-	-	0.2
83	DD2	[20]	1.5	1.8	full	18.84	15.52	-	-	0.25
84	DD2	[22]	1.25	1.47	fullN	0.42	0.29	-	-	0.3
85	DD2	[23]	1.25	1.45	fullN	5	1.61	-	-	0.19
86	DD2	[20]	1.2	1.35	full	3.17	2.06	-	-	0.2
87	DD2	[20]	1.35	1.5	full	3.57	3.13	-	-	0.25
88	DD2	[23]	1.3	1.4	fullN	3	0.87	-	-	0.18
89	DD2	[20]	2	2	full	0.25	0.25	-	-	0.25
90	DD2	[20]	1.8	1.8	full	1.37	1.63	-	-	0.26
91	DD2	[20]	1.6	1.6	full	7.8	7.4	-	-	0.27
92	DD2	[20]	1.5	1.5	full	5.38	4.66	-	-	0.26
93	DD2	[22]	1.36	1.36	fullN	0.43	0.31	-	-	0.3
94	DD2	[20]	1.35	1.35	2	2.57	3.31	-	-	0.34
95	DD2	[20]	1.35	1.35	1.8	2.26	2.61	-	-	0.32
96	DD2	[20]	1.35	1.35	1.5	2.72	2.9	-	-	0.3
97	DD2	[20]	1.35	1.35	full	3.07	2.18	-	-	0.22
98	DD2	[23]	1.35	1.35	fullN	2	0.46	-	-	0.16
99	DD2	[20]	1.2	1.2	full	3.09	1.37	-	-	0.17
100	ENG	[20]	1.35	1.35	2	5.29	5.01	-	-	0.29
101	ENG	[20]	1.35	1.35	1.5	6.32	5.3	-	-	0.26
102	Glenh3	[20]	1.35	1.35	2	1.08	0.62	-	-	0.23
103	Glenh3	[20]	1.35	1.35	1.5	1.69	0.9	-	-	0.22
104	GS2	[20]	1.2	1.5	full	10.69	6.14	-	-	0.18
105	GS2	[20]	1.35	1.35	full	2.74	2.16	-	-	0.19
106	H3	[20]	1.35	1.35	2	1.43	1.15	-	-	0.27
107	H4	[21]	1.25	1.45	1.75	6	2.8	-	-	0.23
108	H4	[20]	1.35	1.35	2	1.28	1.09	-	-	0.27
109	H4	[21]	1.35	1.35	1.75	0.6	0.5	-	-	0.3
110	H4	[20]	1.35	1.35	1.5	1.93	1.64	-	-	0.27
111	MPA1	[20]	1.35	1.35	2	3.64	3.6	-	-	0.3
112	MPA1	[20]	1.35	1.35	1.5	4.48	4.35	-	-	0.29
113	MS1	[21]	1.25	1.45	1.75	5.8	1.2	-	-	0.15
114	MS1	[20]	1.35	1.35	2	1.17	0.98	-	-	0.27

115	MS1	[21]	1.35	1.35	1.75	0.7	0.2	-	-	0.18
116	MS1	[20]	1.35	1.35	1.5	2.38	1.19	-	-	0.21
117	MS1b	[20]	1.35	1.35	2	1.67	1.26	-	-	0.25
118	MS1b	[20]	1.35	1.35	1.5	3.64	1.85	-	-	0.21
119	MS2	[20]	1.35	1.35	2	0.81	0.65	-	-	0.26
120	NL3	[20]	1.2	1.8	full	15.68	5.75	-	-	0.15
121	NL3	[20]	1.35	2	full	12.85	7.62	-	-	0.2
122	NL3	[20]	1.35	1.8	full	18.81	11.31	-	-	0.21
123	NL3	[20]	1.2	1.6	full	9.96	5.57	-	-	0.19
124	NL3	[20]	1.2	1.5	full	7.95	4.5	-	-	0.19
125	NL3	[20]	1.5	1.8	full	8.1	4.94	-	-	0.21
126	NL3	[22]	1.25	1.47	fullN	2.3	1.22	-	-	0.25
127	NL3	[20]	1.35	1.5	full	2.72	2.25	-	-	0.24
128	NL3	[20]	1.2	1.35	full	4.25	2.74	-	-	0.21
129	NL3	[20]	2	2	full	1.91	2.18	-	-	0.29
130	NL3	[20]	1.8	1.8	full	9.08	7.25	-	-	0.24
131	NL3	[20]	1.6	1.6	full	3.74	2.59	-	-	0.22
132	NL3	[20]	1.5	1.5	full	1.7	1.04	-	-	0.2
133	NL3	[22]	1.36	1.36	fullN	0.015	0.01	-	-	0.45
134	NL3	[20]	1.35	1.35	2	1.57	2.03	-	-	0.34
135	NL3	[20]	1.35	1.35	1.8	1.6	2.99	-	-	0.32
136	NL3	[20]	1.35	1.35	1.5	1.86	1.98	-	-	0.3
137	NL3	[20]	1.35	1.35	full	2.09	0.98	-	-	0.18
138	NL3	[20]	1.2	1.2	full	2.15	0.91	-	-	0.17
139	SFHo	[20]	1.2	1.8	full	5.78	10.08	-	-	0.34
140	SFHo	[20]	1.35	1.8	full	11.76	16.22	-	-	0.31
141	SFHo	[20]	1.2	1.6	full	16.91	11.1	-	-	0.21
142	SFHo	[20]	1.2	1.5	full	13.39	8.94	-	-	0.22
143	SFHo	[20]	1.5	1.8	full	6.34	14.4	-	-	0.42
144	SFHo	[22]	1.25	1.47	fullN	2.2	1.8	-	-	0.25
145	SFHo	[23]	1.25	1.45	fullN	11	5.66	-	-	0.24
146	SFHo	[20]	1.2	1.35	full	5.44	3.86	-	-	0.22
147	SFHo	[20]	1.35	1.5	full	18.73	13.34	-	-	0.23
148	SFHo	[23]	1.3	1.4	fullN	6	2.15	-	-	0.2
149	SFHo	[23]	1.33	1.37	fullN	9	3.55	-	-	0.21
150	SFHo	[20]	1.8	1.8	full	0.17	0.24	-	-	0.29
151	SFHo	[20]	1.6	1.6	full	1.13	1	-	-	0.21
152	SFHo	[20]	1.5	1.5	full	4.1	4.13	-	-	0.27
153	SFHo	[22]	1.36	1.36	fullN	3.4	1.8	-	-	0.25
154	SFHo	[20]	1.35	1.35	2	2.96	3.37	-	-	0.32
155	SFHo	[20]	1.35	1.35	1.8	3.26	4.18	-	-	0.34
156	SFHo	[20]	1.35	1.35	1.5	3.82	4.14	-	-	0.3
157	SFHo	[20]	1.35	1.35	full	4.83	3.61	-	-	0.23
158	SFHo	[23]	1.35	1.35	fullN	11	4.76	-	-	0.22
159	SFHo	[20]	1.2	1.2	full	1.88	1.26	-	-	0.21
160	SFHx	[20]	1.2	1.5	full	14.67	7.91	-	-	0.19
161	SFHx	[20]	1.35	1.35	full	6.16	4.36	-	-	0.22
162	SLy	[21]	1.25	1.45	1.75	6.5	5.1	-	-	0.3
163	SLy	[21]	1.35	1.35	1.75	12.2	7.1	-	-	0.26
164	SLy4	[20]	1.35	1.35	2	3.99	3.75	-	-	0.29
165	SLy4	[20]	1.35	1.35	1.5	6.4	5.53	-	-	0.27
166	TM1	[20]	1.2	1.5	full	8.66	3.94	-	-	0.17
167	TM1	[20]	1.35	1.35	2	1.37	2.02	-	-	0.36

168	TM1	[20]	1.35	1.35	1.8	1.33	1.77	-	-	0.34
169	TM1	[20]	1.35	1.35	1.5	1.53	1.86	-	-	0.32
170	TM1	[20]	1.35	1.35	full	1.67	0.74	-	-	0.16
171	TMA	[20]	1.2	1.5	full	10.21	6.4	-	-	0.2
172	TMA	[20]	1.35	1.35	full	2.05	1.19	-	-	0.18

3. Ejecta properties

3.1. Ejecta mass

Considering EM signals from BNS mergers, one of the most important quantities influencing the luminosity of kilonovae and radio flares is the mass of the material ejected from the system. The authors in [27, 28] proposed fitting formulas for the disk and ejecta mass for BHNS systems. To our knowledge no fit for the mass of the ejected material for BNS mergers exists to date.

Our fitting formula

$$\frac{M_{\text{ej}}^{\text{fit}}}{10^{-3}M_{\odot}} = \left[a \left(\frac{M_2}{M_1} \right)^{1/3} \left(\frac{1 - 2C_1}{C_1} \right) + b \left(\frac{M_2}{M_1} \right)^n + c \left(1 - \frac{M_1}{M_1^*} \right) \right] M_1^* + (1 \leftrightarrow 2) + d. \quad (1)$$

is an extension of the work done for BHNS systems to a system consisting of two neutron stars. We denote the mass in isolation of the i -th star as M_i , the baryonic mass as M_i^* , and the compactness as C_i . Let us emphasize that although it has been shown that for BNS mergers a significant part of the ejecta is produced by shocks, e.g., [19], (1) gives a robust estimate for the ejecta for almost all considered configurations. For our data we obtain the following fitting parameters:

$$a = -1.35695, \quad b = 6.11252, \quad c = -49.43355, \quad d = 16.1144, \quad n = -2.5484. \quad (2)$$

The left panels of figure 2 show our results for the ejecta mass. In the upper panel we present M_{ej} for the numerical simulation (blue circles) and for our fitting formula $M_{\text{ej}}^{\text{fit}}$ (red crosses). Both quantities are plotted as a function of the simulation-ID introduced in table 1. The bottom panel shows the absolute residual $\Delta M_{\text{ej}} = M_{\text{ej}}^{\text{fit}} - M_{\text{ej}}$. We include as shaded regions the 1σ ($\Delta M_{\text{ej}}^{1\sigma} = 4.4 \times 10^{-3}M_{\odot}$) and 2σ confidence intervals. Our model function has an average residual of $\Delta \bar{M}_{\text{ej}} = 2.9 \times 10^{-3}M_{\odot}$, which corresponds to a fractional error of $\sim 72\%$.

Overall, because of the difficulties computing the ejecta properties, see section 2, $\Delta \bar{M}_{\text{ej}}$ is of the same order as the numerical uncertainty of the NR data points and therefore can be considered as a possible estimate.

Additionally, we present the results obtained from the fit in Fig. 3, where the absolute and relative difference between the NR data and the fit are shown as a function of the mass ratio and the compactnesses of the stars. Obviously for equal mass setups the relative difference is larger because of the smaller ejecta mass. Those setups also have the highest NR uncertainty. Considering the influence of the compactnesses, we find that for larger compactness of the lighter star the absolute error increases.

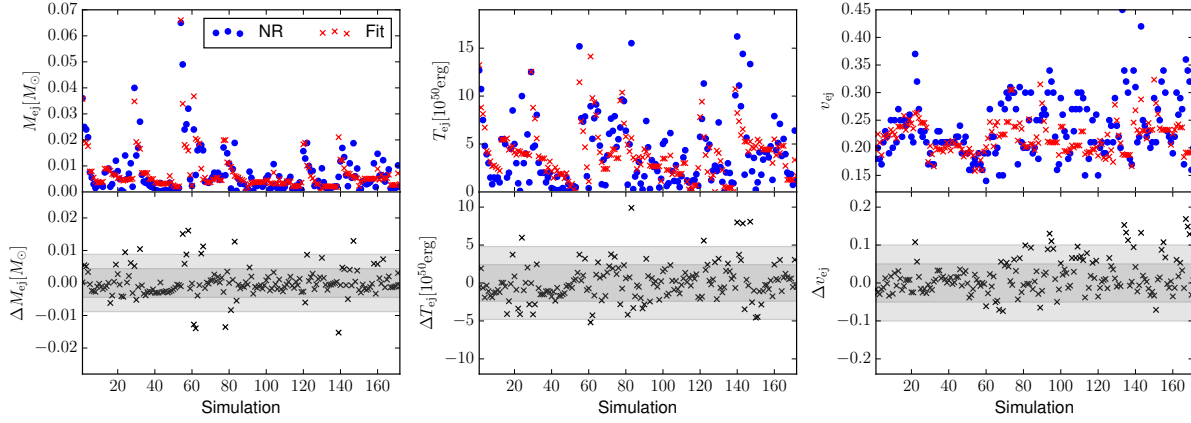


Figure 2. From left to right: ejecta mass M_{ej} , kinetic energy of the ejecta T_{ej} , and velocity of the ejecta v_{ej} . The top panels show the NR data and the results obtained by our phenomenological fits. The bottom panels show the absolute difference between the fit and the NR data, as shaded regions we also include the 1- σ and 2- σ confidence interval.

Let us also mention the possibility of obtaining fits for the ejecta mass (and other quantities) which are independent of the compactness of the stars and solely depend on the mass and tidal deformability, i.e. on quantities directly accessible by a GW observation without assuming an EOS. One possibility might be the usage of quasi-universal compactness-Love relations as mentioned in [29] to substitute the compactness in (1), also the baryonic mass could be represented by the gravitational mass with introducing deviations to the NR only slightly larger than those of the current fits \ddagger . We are not following this approach here, since it did not allowed a better representation of the NR data and we tend to stay closer to the work previously presented for BHNSs systems.

3.2. Kinetic energy

To estimate the kinetic energy of the ejecta we use a similar approach as for the unbound mass, i.e.,

$$\frac{T_{\text{ej}}^{\text{fit}}}{10^{50} \text{erg}} = \left[a \left(\frac{M_2}{M_1} \right)^{1/3} \left(\frac{1 - 2C_1}{C_1} \right) + b \left(\frac{M_2}{M_1} \right)^n + c \left(1 - \frac{M_1}{M_1^*} \right) \right] M_1^* + (1 \leftrightarrow 2) + d. \quad (3)$$

The fitting parameters for the kinetic energy are:

$$a = -1.94315, \quad b = 14.9847, \quad c = -82.0025, \quad d = 4.75062, \quad n = -0.87914. \quad (4)$$

The average residual between our fit and the pure NR data is $\Delta \bar{T}_{\text{ej}} = 1.74 \times 10^{50} \text{erg}$, which corresponds to a difference of 79%. Thus, the kinetic energy is slightly worse represented by our fit than the ejecta mass. The middle panels of figure 2 represent

\ddagger We thank Nathan K. Johnson-McDaniel for pointing this out.

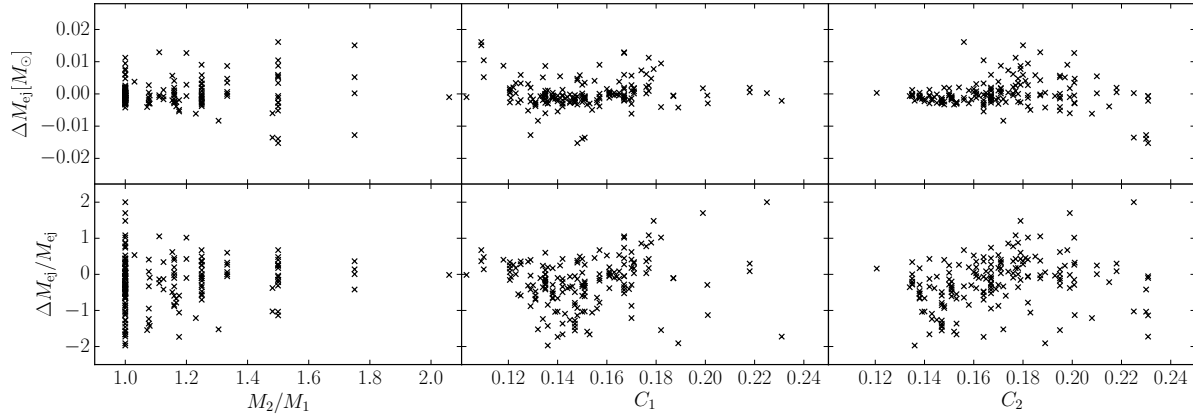


Figure 3. Difference between the ejecta mass of the NR simulation and the proposed fit. Top panels show the absolute difference $\Delta M_{\text{ej}} = M_{\text{ej}}^{\text{NR}} - M_{\text{ej}}^{\text{fit}}$ between the fit and the NR data and bottom panels the relative difference $2\Delta M_{\text{ej}} / (M_{\text{ej}}^{\text{NR}} + M_{\text{ej}}^{\text{fit}})$.

our results for the kinetic energy, where again the 1σ and 2σ intervals are included ($\Delta T_{\text{ej}}^{1\sigma} = 2.4 \times 10^{50} \text{erg}$).

3.3. Ejecta velocities

For the velocity we simplify our fitting function and restrict our analysis to the first 66 data points in table 1. For these data points the velocities inside the orbital plane and perpendicular to it are given. For BHNSs it is known that the velocity depends linearly on the mass ratio of the system, see [28]. It was shown in [24] that the same functional dependence holds for BNSs with high mass ratio or systems employing a stiff EOS. However, shock produced ejecta have a higher velocity component orthogonal to the orbital plane and should be included for a reliable estimate. Thus, we introduce an EOS dependent fitting function by including a first order polynomial depending on the compactness $(1 + c C_{1,2})$, which leads to

$$v_{\rho} = \left[a \left(\frac{M_1}{M_2} \right) (1 + c C_1) \right] + (1 \leftrightarrow 2) + b. \quad (5)$$

The parameters are:

$$a = -0.219479, \quad b = 0.444836, \quad c = -2.67385. \quad (6)$$

Employing these parameters the NR data are represented with an average error of $\Delta \bar{v}_{\rho} = 0.020$, which corresponds to a percentile difference of 13%.

The same expression is used for the velocity orthogonal to the orbital plane:

$$v_z = \left[a \left(\frac{M_1}{M_2} \right) (1 + c C_1) \right] + (1 \leftrightarrow 2) + b. \quad (7)$$

As discussed, e.g., [19], torque produced ejecta have much smaller velocities perpendicular to the orbital plane than inside the orbital plane. Thus, mostly shock

driven ejecta cause large velocities orthogonal to the orbital plane. The parameters we obtain for v_z are:

$$a = -0.315585, \quad b = 0.63808, \quad c = -1.00757 \quad (8)$$

with average residuals of $\Delta v_z = 0.013$ and a fractional difference of 33%. The fractional difference is larger than for v_ρ since the absolute value of the velocities is smaller.

From v_ρ and v_z we estimate the total ejecta velocity as

$$v_{\text{ej}} = \sqrt{v_\rho^2 + v_z^2}. \quad (9)$$

To check our description of v_{ej} we compare all data points (including the remaining 105 data points for which only the total ejecta velocity v_{ej} is known) to our fits. In total we obtain average residuals of $\Delta \bar{v}_{\text{ej}} = 0.036$ and an average percentile uncertainty of 15%. Figure 2 (right panels) shows the ejecta velocities. We find that the residuals are smaller for the 66 data points which we used to obtain the fits of v_ρ, v_z than for the remaining 105 data points. Overall one sees that the phenomenological fit slightly underestimates the velocity.

3.4. Other quantities

3.4.1. Geometry: The geometry of the ejecta can be extracted from NR simulations by considering 3D volume data of the density, but those data are not accessible for most of the configurations presented in table 1. Thus, we want to present in the following a model for homogeneously distributed material inside an annular sector moving with the velocity v_{ej} . Inside the $\rho - z$ -plane the ejecta is distributed in a circular sector with a polar opening angle $2\theta_{\text{ej}}$. The ejected material has an azimuthal opening angle of ϕ_{ej} . Under the assumption that the ejecta consists of particles moving radially outward with velocity v_{ej} , we obtain by averaging over all particles the following equations for v_ρ and v_z :

$$v_\rho \approx v_{\text{ej}} \frac{\sin(\theta_{\text{ej}})}{\theta_{\text{ej}}}, \quad v_z \approx v_{\text{ej}} \frac{1 - \cos(\theta_{\text{ej}})}{\theta_{\text{ej}}}. \quad (10)$$

For a non-zero, but small θ_{ej} one gets

$$\frac{\theta_{\text{ej}}^3}{24} + \frac{\theta_{\text{ej}}}{2} - \frac{v_z}{v_\rho} \approx 0, \quad (11)$$

which can be solved for θ_{ej} :

$$\theta_{\text{ej}} \approx \frac{-2^{4/3}v_\rho^2 + 2^{2/3}(v_\rho^2(3v_z + \sqrt{9v_z^2 + 4v_\rho^2}))^{2/3}}{(v_\rho^5(3v_z + \sqrt{9v_z^2 + 4v_\rho^2}))^{1/3}}. \quad (12)$$

In contrast to the opening angle θ_{ej} , it is more difficult from our current results to estimate the azimuthal angle ϕ_{ej} . In [28] was assumed that BHNS setups have an azimuthal angle of $\phi_{\text{ej}} \approx \pi$. This is in agreement with high mass ratio BNS

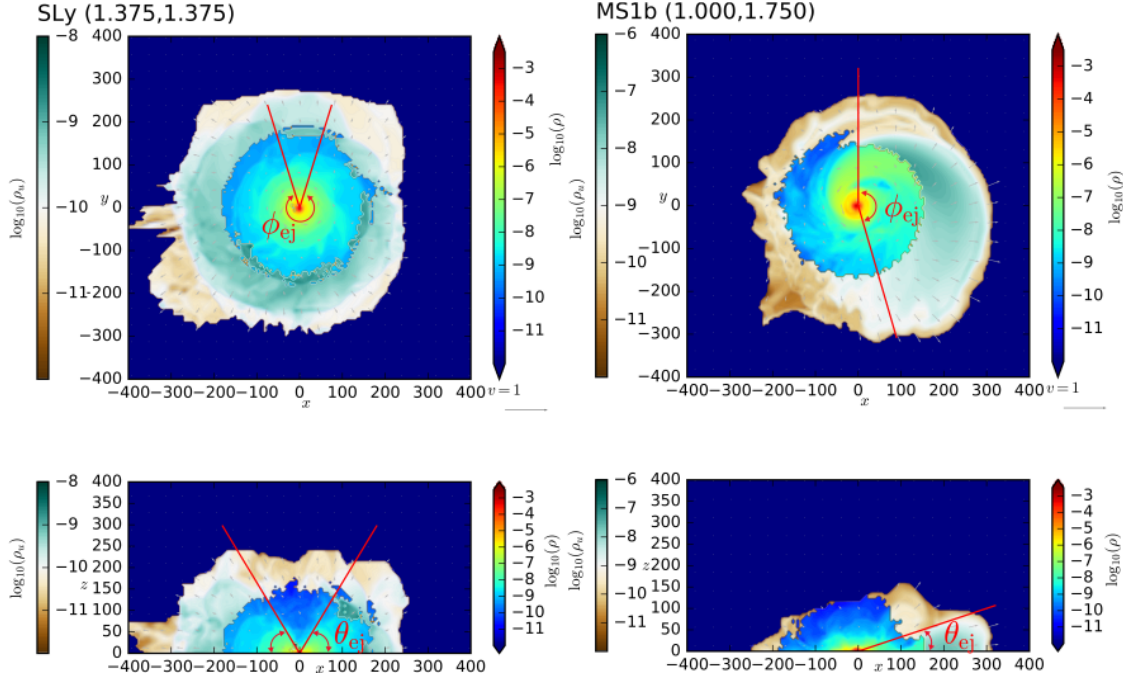


Figure 4. 2D density plots with rest mass ρ shown from blue to red with increasing density and the unbound material ρ_u shown brown to green with increasing density. Geometric units are employed. We use the velocity as extracted from the numerical simulation and show θ_{ej} and ϕ_{ej} as approximated from (12) and (13). Left: Simulations #66 (SLy, $1.375M_{\odot}, 1.375M_{\odot}$) Right: Simulation #55 (MS1b, $1.000M_{\odot}, 1.750M_{\odot}$).

mergers employing stiff EOSs [24], i.e. for setups where torque is the dominant ejection mechanism. Contrary if shock ejecta are present, e.g. for softer EOSs, the azimuthal angle even increases up to 2π , i.e. there exists a correlation between θ_{ej} and ϕ_{ej} . Assuming that the opening angles vary between $\theta_{\text{ej}} \in [\pi/8, 3\pi/8]$ and $\phi_{\text{ej}} \in [\pi, 2\pi]$, and that θ_{ej} and ϕ_{ej} are linearly correlated, we obtain

$$\phi_{\text{ej}} = 4\theta_{\text{ej}} + \frac{\pi}{2}. \quad (13)$$

To test our approximations, we present snapshots of the density profile in the x - y and x - z plane for the simulations #55 and #66 in figure 4. We show the rest-mass density ρ (color bar ranging from blue to red) and the unbound rest mass density ρ_u (color bar ranging from brown to green). The two cases present two rather extreme setups, namely a stiff EOS with a large mass ratio and a soft EOS for an equal mass system. In figure 4 we also include the approximations for θ_{ej} and ϕ_{ej} obtained from (12) and (13). The examples show that the geometry of the higher density ejecta regions can be described reasonably well with our model.

3.4.2. Composition: Caused by different ejecta mechanisms the composition and electron fraction of the ejecta varies depending on the EOS, mass ratio, and total mass. As pointed out in the literature, unbound material ejected due to torque in the tidal

Table 2. Columns refer to: The data ID as in table 1, the mass of the first star M_1 , the mass of the second star M_2 , the ejecta mass M_{ej} , the kinetic energy of ejecta T_{ej} , the ejecta velocity v_{ej} , and the electron fraction Y_e . All setups have been simulated in [23].

#	EOS	M_1 [M_\odot]	M_2 [M_\odot]	M_{ej} [$10^{-3}M_\odot$]	T_{ej} [10^{50}erg]	v_{ej} [c]	Y_e
85	DD2	1.25	1.45	5	1.61	0.19	0.2
88	DD2	1.3	1.4	3	0.87	0.18	0.26
98	DD2	1.35	1.35	2	0.46	0.16	0.3
145	SFHo	1.25	1.45	11	5.66	0.24	0.18
148	SFHo	1.3	1.4	6	2.15	0.2	0.27
149	SFHo	1.33	1.37	9	3.55	0.21	0.3
158	SFHo	1.35	1.35	11	4.76	0.22	0.31

tail of the NSs has a low electron fraction, see e.g., [30]. Contrary ejecta produced via shock heating have overall a broader range in electron fraction, e.g., [23]. Table 2 shows the fraction of data from table 1 for which we also know the average electron fraction. Note that the electron fraction of the ejected material varies significantly among different implementations for the neutrino transport, e.g., [31, 32, 22] find overall smaller electron fractions of the unbound material than reported in [23]. Consequently the presented results have to be taken with care and the following should be regarded as a qualitative discussion.

Figure 5 summarized the important results from table 2. As shown in figure 1 the DD2 EOS is softer than SFHo. Considering the left panel of figure 5 we observe that for both EOSs an increasing mass ratio leads to a smaller electron fraction. This is expected since more ejecta are produced due to torque independent of the EOS. The right panel shows the dependence between the ejecta mass and the electron fraction. For all setups more massive ejecta are produced for the softer EOS, e.g., for $q = 1$ more than five times more mass is ejected for the SFHo EOS. For this mass ratio the dominant ejection mechanism for SFHo is shock heating, which seems to be suppressed for increasing mass ratios. Thus, the ejecta mass and the electron fraction decreases for increasing q (see also the explanation in [23]). Interestingly is that while for DD2 $Y_e(M_{\text{ej}})$ is monotonic, this is not true for SFHo, where beyond a mass ratio of $q \approx 1.1$ the ejecta mass is growing again. We propose that for $q > 1.1$ also SFHo setups become dominated by torque produced ejecta and shocks are suppressed.

Finalizing our consideration of the composition, we want to present a fit for the electron fraction as a function of the mass ratio for a total mass of $M = 2.7M_\odot$ for the data of [23]:

$$Y_e = 0.306 - 0.318(q - 1) - 2.568(q - 1)^2. \quad (14)$$

The fit is shown as a black dashed line in figure 5 (left panel). To generalize (14) to different total masses and higher mass ratios more simulations including realistic

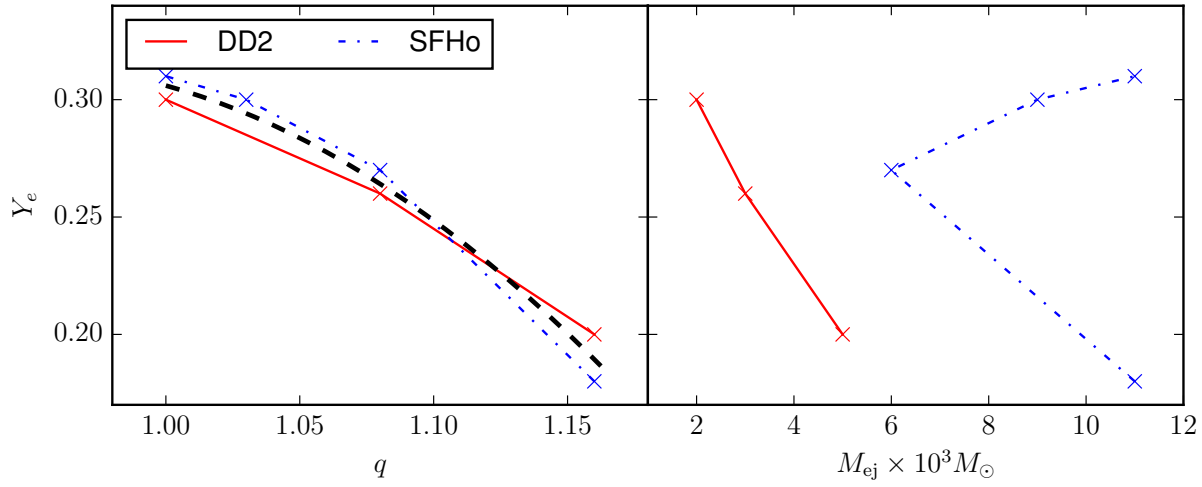


Figure 5. Left panel: Electron fraction Y_e as a function of the mass ratio q . Right panel: Electron fraction Y_e as a function of the ejecta mass M_{ej} . We present data for two different EOSs: SFHo (blue dashed dotted line) and the stiffer DD2 (red solid line). In the left panel we also include as a black dashed line the fit of (14).

microphysical treatments are required.

3.4.3. Spin effects: Let us also briefly comment on the effect of the star’s intrinsic rotation on the ejecta quantities. We summarize in tab. 3 the spinning configurations of [33]. Figure 6 visualizes these data and shows the influence of the mass ratio and of the spin of the secondary (less massive star) on the ejecta mass. The figure shows two distinct effects (i) for an increasing mass ratio more material becomes unbound (as already discussed above), (ii) if the spin of the secondary star is aligned to the orbital angular momentum (positive) then the ejecta mass increases even further.

As pointed out in [33] spin aligned to the orbital angular momentum enhances the ejection, while contrary antialigned spin leads to lower massive ejecta. This can be understood by considering the fluid velocity inside the tidal tail, which at lowest order can be approximated as the sum of the orbital fluid velocity and the fluid velocity connected to the intrinsic rotation of the star. In cases where the individual star also has spin parallel to the orbital angular momentum the fluid velocity inside the tail is higher and consequently material gets unbound and leaves the system. This effect becomes most prominent for systems for which material ejection is caused by torque, e.g. by unequal mass systems. Because in unequal mass systems the mass ejection happens mostly from the tidal tail of the lower massive star, the determining quantity is the spin of the secondary star χ_2 as shown in figure 6.

4. Kilonovae

It is expected that the ejected material is heated up because of the radioactive decay of r-process elements and consequently triggers EM emission called kilo- or macronovae,

Table 3. Overview about the spinning simulations taken from [33]. The columns refer to: EOS, individual masses $M_{1,2}$, dimensionless spins of the stars $\chi_{1,2}$, the ejecta mass M_{ej} , kinetic energy of the ejecta T_{ej} , velocity inside the orbital plane v_ρ and perpendicular to it v_z .

EOS	M_1 [M_\odot]	χ_1	M_2 [M_\odot]	χ_2	M_{ej} [$10^{-3}M_\odot$]	T_{ej} [10^{50}erg]	v_ρ [c]	v_z [c]
ALF2	1.375	0.102	1.375	-0.102	4.1	0.55	0.12	0.07
ALF2	1.375	0.102	1.375	0.000	2.0	0.36	0.13	0.05
ALF2	1.375	0.102	1.375	0.102	1.6	0.32	0.16	0.05
ALF2	1.528	0.104	1.223	-0.102	4.5	1.7	0.15	0.11
ALF2	1.528	0.104	1.222	0.000	5.5	2.1	0.16	0.13
ALF2	1.528	0.104	1.223	0.102	6.7	2.	0.16	0.08
ALF2	1.651	0.107	1.100	-0.101	11	3.6	0.18	0.05
ALF2	1.651	0.107	1.100	0.000	14	4.1	0.18	0.04
ALF2	1.651	0.107	1.100	0.101	24	7.5	0.18	0.04
H4	1.375	0.100	1.375	-0.100	1.5	0.62	0.16	0.10
H4	1.375	0.100	1.375	0.000	0.7	0.23	0.17	0.10
H4	1.375	0.100	1.375	0.100	2.0	0.78	0.15	0.07
H4	1.528	0.100	1.223	-0.100	4.1	1.7	0.17	0.09
H4	1.528	0.100	1.222	0.000	6.4	3.2	0.18	0.08
H4	1.528	0.100	1.223	0.100	7.8	3.0	0.18	0.11
H4	1.651	0.101	1.100	-0.099	9.5	2.4	0.17	0.03
H4	1.651	0.101	1.100	0.000	19	5.5	0.17	0.03
H4	1.651	0.101	1.100	0.099	27	7.5	0.17	0.02

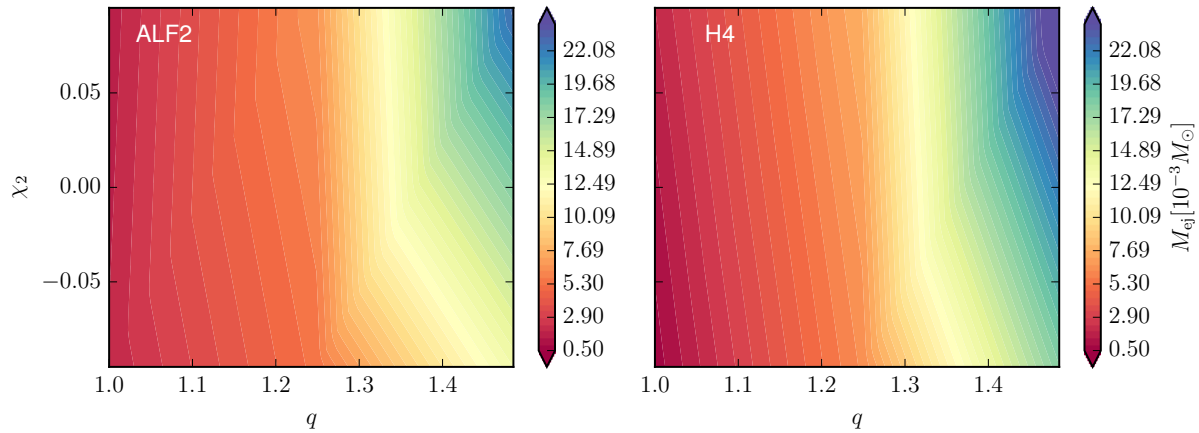


Figure 6. Ejecta mass for the spinning configurations of table 3 as a function of the mass ratio q and the spin of the secondary star χ_2 for the ALF2 EOS (left) and the H4 EOS (right).

see among others [34, 35, 36, 12, 8, 37, 14, 15, 38, 39] and for overview articles [40, 25]. Up to date there are three possible kilonovae candidates for which a connection to a GRB has been made: GRB 050709 [10], GRB 060614 [9], GRB 130603B [8]. The most

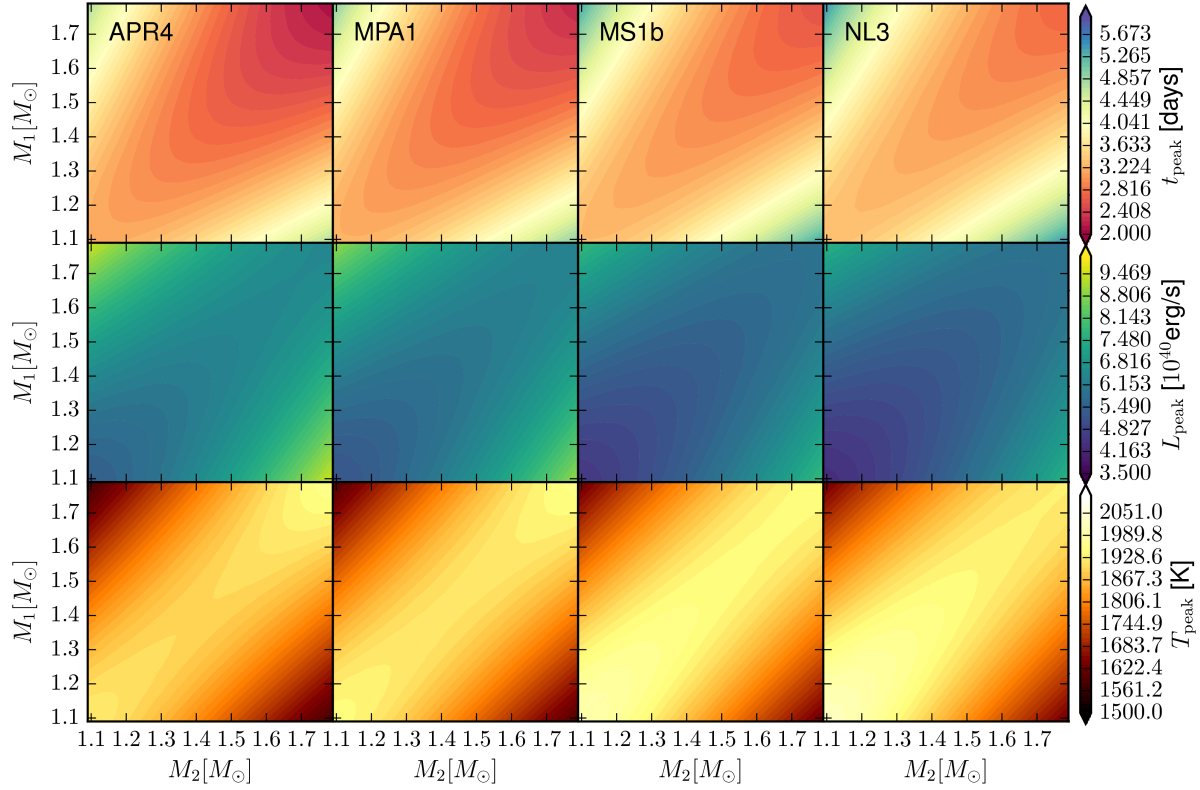


Figure 7. Kilonovae properties: upper panel shows the time when the peak luminosity is reached; middle panels show the corresponding luminosity, and the bottom panel the corresponding temperature. We present results for four different EOSs, from left to right: APR4, MPA1, MS1b, NL3, i.e., the compactness is from left to right decreasing, see figure 1. The quantities are given in terms of the individual masses of the stars M_1, M_2 .

likely origin of these kilonovae candidates are compact binary mergers.

4.1. Peak quantities

Based on the work of [14] we will present some important kilonovae properties. The time t_{peak} at which the peak in the near-infrared occurs, the bolometric luminosity at this time L_{peak} , and the corresponding temperature T_{peak} are given as:

$$t_{\text{peak}} = 4.9 \text{ days} \times \left(\frac{M_{ej}}{10^{-2} M_\odot} \right)^{\frac{1}{2}} \left(\frac{\kappa}{10 \text{ cm}^2 \text{ g}^{-1}} \right)^{\frac{1}{2}} \left(\frac{v_{ej}}{0.1} \right)^{-\frac{1}{2}}, \quad (15a)$$

$$L_{\text{peak}} = 2.5 \cdot 10^{40} \text{ erg s}^{-1} \times \left(\frac{M_{ej}}{10^{-2} M_\odot} \right)^{1-\frac{\alpha}{2}} \left(\frac{\kappa}{10 \text{ cm}^2 \text{ g}^{-1}} \right)^{-\frac{\alpha}{2}} \left(\frac{v_{ej}}{0.1} \right)^{\frac{\alpha}{2}}, \quad (15b)$$

$$T_{\text{peak}} = 2200 \text{ K} \times \left(\frac{M_{ej}}{10^{-2} M_\odot} \right)^{-\frac{\alpha}{8}} \left(\frac{\kappa}{10 \text{ cm}^2 \text{ g}^{-1}} \right)^{-\frac{\alpha+2}{8}} \left(\frac{v_{ej}}{0.1} \right)^{\frac{\alpha-2}{8}}. \quad (15c)$$

In [14] the authors assume that the energy release due to the radioactive decay is proportional to $\sim t^{-\alpha}$ with $\alpha = 1.3$. We set the average opacity to $\kappa = 10 \text{ cm}^2\text{g}^{-1}$ §.

In figure 7 we present $t_{\text{peak}}, L_{\text{peak}}, T_{\text{peak}}$ for four different EOSs as a function of the individual masses M_1, M_2 . We find for all setups that an increasing mass-ratio increases $t_{\text{peak}}, L_{\text{peak}}$ and decreases T_{peak} . Furthermore an increasing total mass leads to a decreasing t_{peak} . Considering the influence of the EOS, softer EOSs lead to more luminous kilonovae in particular for equal mass merger. This can be explained by smaller ejecta mass caused by the absence of shock driven ejecta for stiff EOSs. For systems close to equal mass the temperature of the kilonovae is higher. Interesting is also that for equal mass systems the luminosity and the temperature have saddle points, see middle and lower panels. This means that keeping the mass ratio fixed a local extrema exist for which the luminosity becomes maximal and that also a local extrema exists for which the temperature becomes minimal. Both points do not have to coincide. It would be interesting to test with further NR simulations whether such a saddle point exists or is just an artifact of the employed fit.

4.2. Time evolution

4.2.1. Luminosity: To determine the luminosity of the kilonovae, we follow the discussion of [28], which we briefly summarize below. As described in section 3.4.1 the ejecta is modeled as a partial sphere in the latitudinal and longitudinal direction. We further assume that the material is homogeneously distributed inside the ejecta and that photons purely escape from the latitudinal edge. This agrees with the assumptions made in [28] and also gives valid results for BNS mergers as shown below. Considering that the optical depth increases with decreasing density, the whole region becomes visible after

$$t_c = \sqrt{\frac{\theta_{\text{ej}} \kappa M_{\text{ej}}}{2\phi_{\text{ej}}(v_{\text{max}} - v_{\text{min}})}}, \quad (16)$$

with $v_{\text{max}}, v_{\text{min}}$ being the maximum and the minimum speed of the ejecta. The mass of the photon escaping region is then given by $M_{\text{obs}} = M_{\text{ej}}(t/t_c)$ for times $t < t_c$. In [37, 42] was shown that the specific heating for energy release caused by radioactive decay can be approximated by $\dot{\epsilon} \approx \dot{\epsilon}_0 \left(\frac{t}{1\text{day}}\right)^{-\alpha}$. This allows to write the bolometric luminosity as

$$L(t) = (1 + \theta_{\text{ej}})\epsilon_{\text{th}}\dot{\epsilon}_0 M_{\text{ej}} \begin{cases} \frac{t}{t_c} \left(\frac{t}{1\text{day}}\right)^{-\alpha}, & t \leq t_c \\ \left(\frac{t}{1\text{day}}\right)^{-\alpha}, & t > t_c \end{cases}, \quad (17)$$

where we will use $\dot{\epsilon}_0 = 1.58 \times 10^{10} \text{ erg g}^{-1} \text{ s}^{-1}$ and $\alpha = 1.3$ for our considerations ||.

§ Notice that as shown in e.g., [15, 41] the typical opacity for a kilonovae is significantly higher than for typical supernovae explosions, which is caused by the presence of lanthanides. The exact value of the opacity depends on the composition of the material, which is not included in our models.

|| Note that as discussed in [28] (17) also used the assumption of a small opening angle θ_{ej} which is valid for BHNSs but might be violated for BNS systems. However, figure 8 reveals that reasonable results are also obtained for BNS systems with larger opening angles, see e.g., SLy (1.35,1.35).

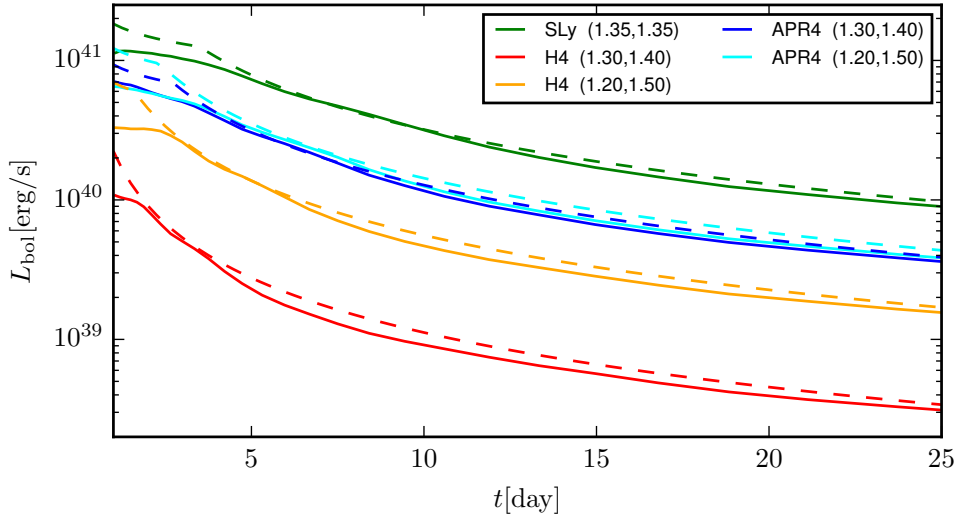


Figure 8. Comparison of the bolometric luminosity given by (17) (dashed lines) and a radiative transfer simulation (solid lines). The results of the radiative transfer simulation was presented in [15, 43] and is public available at [44]. The legend characterizes the EOS and the individual masses of the NSs are given in solar masses.

In figure 8 a comparison between (17) and the radiative transfer simulations of [15, 44] is presented. One sees remarkable agreement between the simple model function and the radiative transfer simulations. As input variables for (17), we have used the stated ejecta masses from [44]. This is necessary since L_{bol} depends strongly on M_{ej} such that a difference in M_{ej} produces a large difference in L_{bol} and a comparison would not test the assumptions made for (17), but how (1) approximates this particular setup. Furthermore, v_{min} is set to 0.02, $v_{\text{max}} = 2v_{\text{ej}} - v_{\text{min}}$, and θ_{ej} and ϕ_{ej} are chosen according to (12) and (13). Figure 8 proves that (17), which was originally proposed for BHNS setups in [28] also allows to describe BNS mergers and the time evolution of the kilonovae.

4.2.2. Lightcurves: From the given luminosity the bolometric magnitude can be computed according to:

$$M_{\text{bol}} \approx 4.74 - 2.5 \log_{10} \left(\frac{L_{\text{bol}}}{L_{\odot}} \right), \quad (18)$$

with L_{\odot} denoting the bolometric luminosity of the sun. To compute the magnitude in each wavelength, we have to know the spectra of the kilonovae. One possible approach to compute the spectra is by considering the effective temperature of the photosphere

$$T \approx \left(\frac{L(t)}{\sigma S(t)} \right)^{1/4}, \quad (19)$$

with $S(t)$ being the surface of the latitudal edge, and to assume that the spectrum of a kilonovae can be approximated by a pseudo black body spectrum, e.g., [41].

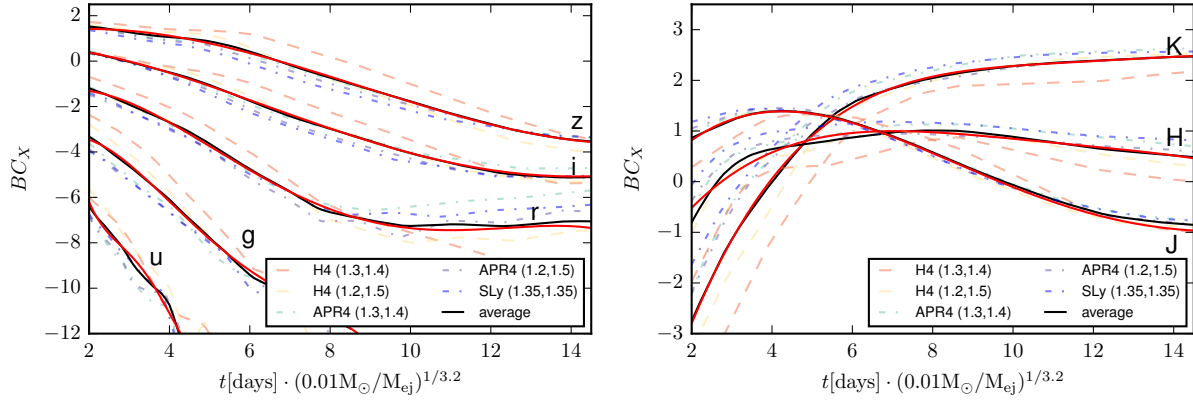


Figure 9. Bolometric corrections for the ugriz-bands (left) and KHJ-bands (right) as a function of the rescaled time $t' = t[\text{days}](0.01M_\odot/M)^{1/3.2}$. We use public available results of [44] and show them as dashed and dot-dashed lines. The average of the available data for each individual band is shown as a black solid line and a fit of the average is visible as a red solid line. The parameters for the fit are given in (22a)-(22h).

Another approach enabling us to compute the spectrum are bolometric corrections (BC) as discussed in [28]. The final magnitude in each band (denoted by the subscript X) is then given by

$$M_X(t) = M_{\text{bol}}(L(t)) - BC_X(t). \quad (20)$$

To compute the bolometric corrections we use the public available light curves of [44]. It was shown in [28] that the time evolution of the BCs for BHNSs agrees once the elapsed time is rescaled by $t' = t \cdot (10^{-2}M_\odot/M_{\text{ej}})^{1/3.2}$. Figure 9 shows that the same rescaling can be used for BNS data. We present for five different setups [44] the BCs for the ugriz-band in the left and for the KHJ-band in the right panel. The difference among the different setups of the BC is about 1 magnitude. To obtain the final BC, we average the results of all five configurations (black solid line) and fit the average with a polynomial (red solid lines)

$$BC_X = a_0 + a_1 t' + a_2 t'^2 + a_3 t'^3 + a_4 t'^4. \quad (21)$$

The final parameters for the polynomials fits are

$$BC_z : (1.072, 0.3646, -0.1032, 0.00368, 0.0000126) \quad t' \in [2, 15] \quad (22a)$$

$$BC_i : (0.6441, 0.0796, -0.122, 0.00793, -0.000122) \quad t' \in [2, 15] \quad (22b)$$

$$BC_r : (-2.308, 1.445, -0.5740, 0.0531, -0.00152) \quad t' \in [2, 15] \quad (22c)$$

$$BC_g : (-6.195, 4.054, -1.754, 0.2246, -0.009813) \quad t' \in [2, 8.5] \quad (22d)$$

$$BC_u : (40.01, -56.79, 25.73, -5.207, 0.3813) \quad t' \in [2, 5] \quad (22e)$$

$$BC_K : (-7.876, 3.245, -0.3946, 0.0216, -0.000443) \quad t' \in [2, 15] \quad (22f)$$

$$BC_H : (-2.763, 1.502, -0.2133, 0.0128, -0.000288) \quad t' \in [2, 15] \quad (22g)$$

$$BC_J : (-1.038, 1.348, -0.2364, 0.0137, -0.000261) \quad t' \in [2, 15]. \quad (22h)$$

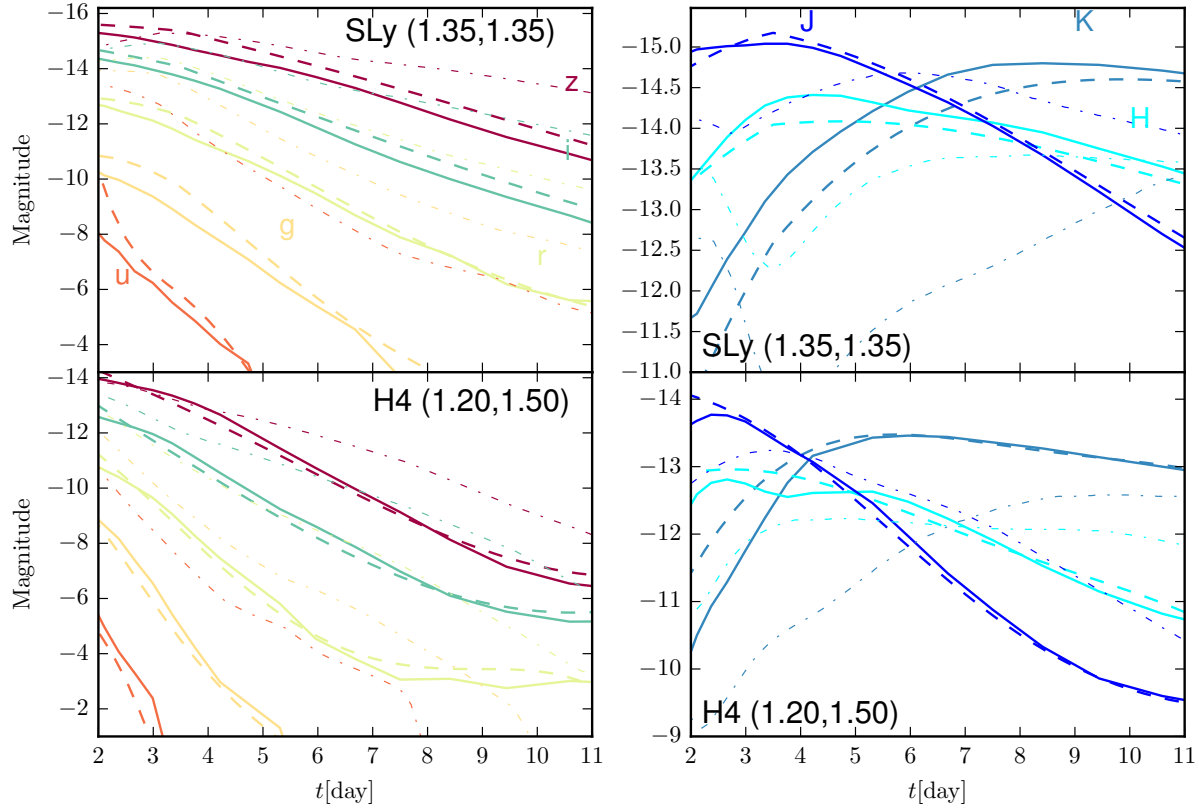


Figure 10. Absolute Magnitudes in the ugriz-bands (left panels) and JHK-bands (right panels) for the equal mass SLy (1.35,1.35) and the unequal mass H4 (1.20,1.50) setups. The solid lines represent the data reported in [15, 44]. The dashed lines represent data obtained from (17) including the computed BC corrections. We also include as a thin dashed dotted line results obtained with the public available code of [45].

As an example we compare the lightcurves obtained from the discussed model and computed with the radiative MC code of [15, 44] for two systems: one equal mass system employing a soft EOS (SLy ($1.35M_{\odot}$, $1.35M_{\odot}$)) and one unequal masses case with a stiffer EOS (H4 ($1.20M_{\odot}$, $1.50M_{\odot}$)). As for figure 8 we use here the ejecta mass stated in [44] to compute the bolometric luminosities. Figure 10 shows that after applying the BCs, the MC results and those obtained by the simple model agree well. Additionally, we also include lightcurves computed with the public available code of [45] (thin dot dashed lines), which was developed for BHNS mergers and which shows a larger disagreement to the MC results. The difference between the MC simulation and the model presented here is smaller because of the particular choice of the BCs.

5. Radio flares

In addition to kilonovae, it is possible that sub-relativistic outflows produce radio flares with peak times of a few month up to years after the merger of the compact binary.

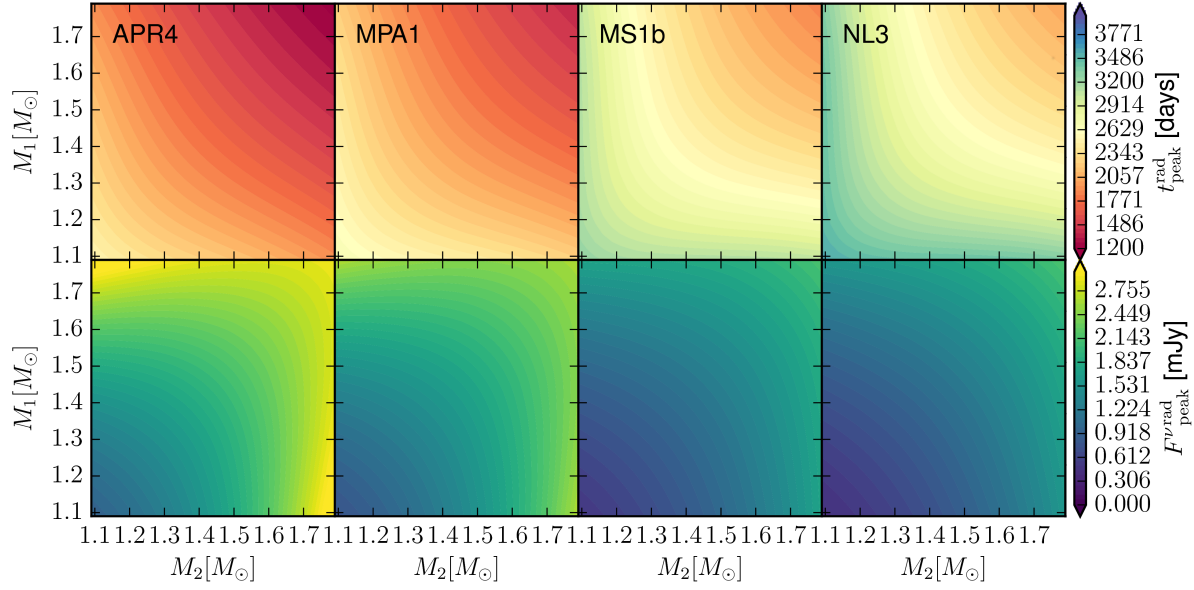


Figure 11. Radio flares properties: upper panel shows the time once the peak in the radio band is observable after the merger of the two neutron stars; lower panel shows the radio fluency at this time. We present results for four different EOSs, from left to right: APR4, MPA1, MS1b, NL3, i.e., the compactness is from left to right decreasing, see figure 1. The quantities are given in terms of the individual masses of the stars M_1, M_2 .

In order to estimate the radio emission, we use the model of [11]. The strongest signal is expected at a time

$$t_{\text{peak}}^{\text{rad}} = 1392 \text{ days} \times \left(\frac{T_{\text{ej}}}{10^{49} \text{ erg}} \right)^{\frac{1}{3}} \left(\frac{n_0}{\text{cm}^{-3}} \right)^{-\frac{1}{3}} \left(\frac{v_{\text{ej}}}{0.1} \right)^{-\frac{5}{3}} \quad (23)$$

after the merger of the system. The radio fluence at this time is

$$F_{\text{peak}}^{\nu \text{rad}} = 0.3 \text{ mJy} \times \left(\frac{T_{\text{ej}}}{10^{49} \text{ erg}} \right) \left(\frac{n_0}{\text{cm}^{-3}} \right)^{\frac{p+1}{4}} \left(\frac{\epsilon_B}{0.1} \right)^{\frac{p+1}{4}} \\ \times \left(\frac{\epsilon_e}{0.1} \right)^{p-1} \left(\frac{v_{\text{ej}}}{1} \right)^{\frac{5p-7}{2}} \left(\frac{D}{10^{27} \text{ cm}} \right)^{-2} \left(\frac{\nu_{\text{obs}}}{1.4 \text{ GHz}} \right)^{-\frac{p-1}{2}} \quad (24)$$

for an observation frequency ν_{obs} higher than the self-absorption and synchrotron peak frequency at a distance D . The parameters ϵ_B and ϵ_e , both set to 0.1, determine how efficient the energy of the blast wave is transferred to the magnetic field and to electrons. n_0 denotes the surrounding particle density and is set to 0.1 cm^{-3} ¶. Additionally we assume $p = 2.3$ and $\nu_{\text{obs}} = 1.4 \text{ GHz}$, as done in [11].

In figure 11 we present for four different EOSs the expected peak time t_{peak} (upper panel) and radio fluence $F_{\text{peak}}^{\nu \text{rad}}$ (lower panel). We find that for an increasing total

¶ Notice that the overall uncertainty on the density of the surrounding material is rather large. To constrain the EOSs or extract the binary parameters from radio observations strict bounds on n_0 will be needed.

mass the peak time $t_{\text{peak}}^{\text{rad}}$ decreases while the peak fluency $F_{\text{peak}}^{\nu\text{rad}}$ increases. For larger mass ratios the peak fluency is largest. Considering different EOSs we find significant differences. In general the observable peak time in the radio band, i.e. $t_{\text{peak}}^{\text{rad}}$, happens later for softer EOSs, for those setups also the peak fluency is higher.

6. Conclusion

6.1. Summary

In this work we have derived fitting functions for the main ejecta properties from binary neutron star mergers, namely the mass, kinetic energy, and velocity of the unbound material. Our work is (as a first step) restricted to dynamical ejecta for which a large number of numerical simulation data are available. In total we use a sample of 172 numerical simulations of binary neutron star mergers to derive our fits. The high number of data points allows to cover a large region of the possible binary neutron star parameter space including 23 different EOSs, total masses between $2.4M_{\odot}$ and $4M_{\odot}$, and mass ratios between $q = 1.0$ and $q \approx 2.1$. The residual errors of the fitting functions are of the order of the uncertainty of the numerical relativity results.

Additionally, we presented estimates for the geometry of the ejected material and compared those with numerical relativity simulations. We found that the high density region of the ejected material can be approximated by a three dimensional annular sector, i.e. a crescent-like structure.

Using the results of [23] we also discussed the influence of the EOS and mass ratio on the electron fraction inside the ejected material, where in general softer and higher mass ratio configurations are characterized by lower electron fractions. Following [33] we presented how the intrinsic rotation on the individual neutron stars affects the ejecta mass, where we found in particular that for high mass ratios the aligned spin of the lower star increases the amount of the ejected material.

Based on estimated ejecta properties we studied possible electromagnetic observables for binary neutron star mergers. In particular, we have focused on the possibility of the formation of kilonovae and radio flares. Considering kilonovae, analytical models have been employed to determine the time when the kilonovae is brightest as well as the corresponding luminosity and temperature. While these estimates just represent the properties of the EM counterpart at a fixed time, we also used the model proposed in [28] to derive the time evolution of the luminosity and light curve. We checked the model against radiative transfer simulations of [44] and found good agreement.

Finally, we estimated the peak time and peak fluency of the radio flares produced after the binary neutron star merger. Those flares will be observable month up to years after the merger.

6.2. Consequences for future observations

The first two GW detections GW150914 and GW151226 have proven that pipelines for EM follow studies are in place and work reliably. Detailed informations can be found in [46] and references therein. However, in case of an upcoming GW detection of a BNS system an estimate about corresponding kilonovae and radio flares may support follow up studies.

Once a GW is detected the first parameter estimates for the binary properties are produced within the first minutes after the detection. This time is small enough to allow observations in the visible, near-infrared, and radio band.

On a practical term it is important to point out that the time between the GW detection and the kilonovae observation is too short to perform full NR simulations, which typically have run times of the order of weeks to months. Thus, once the first knowledge about the properties of the binary is available phenomenological formulas, as presented here, are needed to obtain estimates for possible EM counterparts. After the kilonovae observation NR simulations with microphysical descriptions as neutrinos transport, tabulated EOS, and magnetic fields can be performed to obtain more reliable results. At this stage, our estimates help to reduce the region in the parameter space which have to be covered by NR simulations.

Notice that the situation is different for radio flares, which are detectable on the order of years after the merger. Full-NR simulations for a variety of parameters can be performed between the detection of the GWs and the observation of the radio signal.

Overall, our work represents a first step towards a systematic combination between binary parameters accessible from gravitational wave observations and electromagnetic counterparts for a large range of the binary neutron star parameter space. In the future even more setups have to be included testing extreme corners of the parameter space. Furthermore, a detailed microphysical description in numerical simulations will help to account for other effects as e.g., magnetic fields and the ejecta produced by the disk wind after the formation of the merger remnant.

Acknowledgments

We thank Sebastiano Bernuzzi, Brett Deaton, Francois Foucart, Kyohei Kawaguchi, Nathan K. Johnson-McDaniel, David Radice, Masaomi Tanaka for comments and fruitful discussions.

It is a pleasure to also thank Matthias Hempel who kindly gave us the EOS tables for cold neutron stars in beta-equilibrium. We are grateful to Masaomi Tanaka for making his Monte Carlo simulation data public available and to Kyohei Kawaguchi for making his code to compute lightcurves for BNS systems available.

Parts of the presented results relied on simulations performed on SuperMUC at the LRZ (Munich) under the project number pr48pu, Jureca (Jülich) under the project

number HPO21, Stampede (Texas, XSEDE allocation - TG-PHY140019).

References

- [1] Abbott B P *et al.* (Virgo, LIGO Scientific) 2016 *Phys. Rev. Lett.* **116** 061102 (*Preprint* 1602.03837)
- [2] Abbott B *et al.* (Virgo, LIGO Scientific) 2016 *Phys. Rev. Lett.* **116** 241103 (*Preprint* 1606.04855)
- [3] Aasi J *et al.* (LIGO Scientific Collaboration, Virgo Collaboration) 2016 *Living Rev. Relativity* **19** 1 (*Preprint* 1304.0670)
- [4] Abbott B P *et al.* (Virgo, LIGO Scientific) 2016 (*Preprint* 1607.07456)
- [5] Paczynski B 1986 *Astrophys. J.* **308** L43–L46
- [6] Eichler D, Livio M, Piran T and Schramm D N 1989 *Nature* **340** 126–128
- [7] Soderberg A M *et al.* 2006 *Astrophys. J.* **650** 261–271 (*Preprint* astro-ph/0601455)
- [8] Tanvir N, Levan A, Fruchter A, Hjorth J, Wiersema K *et al.* 2013 *Nature* **500** 547 (*Preprint* 1306.4971)
- [9] Yang B, Jin Z P, Li X, Covino S, Zheng X Z, Hotokezaka K, Fan Y Z, Piran T and Wei D M 2015 *Nature Commun.* **6** 7323 (*Preprint* 1503.07761)
- [10] Jin Z P, Hotokezaka K, Li X, Tanaka M, D’Avanzo P, Fan Y Z, Covino S, Wei D M and Piran T 2016 (*Preprint* 1603.07869)
- [11] Nakar E and Piran T 2011 *Nature* **478** 82–84 (*Preprint* 1102.1020)
- [12] Goriely S, Bauswein A and Janka H T 2011 *Astrophys.J.* **738** L32 (*Preprint* 1107.0899)
- [13] Rosswog S, Korobkin O, Arcones A, Thielemann F K and Piran T 2014 *Mon. Not. Roy. Astron. Soc.* **439** 744–756 (*Preprint* 1307.2939)
- [14] Grossman D, Korobkin O, Rosswog S and Piran T 2014 *Mon. Not. Roy. Astron. Soc.* **439** 757–770 (*Preprint* 1307.2943)
- [15] Tanaka M and Hotokezaka K 2013 *Astrophys.J.* **775** 113 (*Preprint* 1306.3742)
- [16] Hotokezaka K, Kyutoku K, Tanaka M, Kiuchi K, Sekiguchi Y, Shibata M and Wanajo S 2013 *Astrophys. J.* **778** L16 (*Preprint* 1310.1623)
- [17] Faber J A and Rasio F A 2012 *Living Rev.Rel.* **15** 8 (*Preprint* 1204.3858)
- [18] Baiotti L and Rezzolla L 2016 (*Preprint* 1607.03540)
- [19] Hotokezaka K, Kiuchi K, Kyutoku K, Okawa H, Sekiguchi Y *et al.* 2013 *Phys.Rev.* **D87** 024001 (*Preprint* 1212.0905)
- [20] Bauswein A, Goriely S and Janka H T 2013 *Astrophys.J.* **773** 78 (*Preprint* 1302.6530)
- [21] Dietrich T, Bernuzzi S, Ujevic M and Brügmann B 2015 *Phys. Rev.* **D91** 124041 (*Preprint* 1504.01266)
- [22] Lehner L, Liebling S L, Palenzuela C, Caballero O L, O’Connor E, Anderson M and Neilsen D 2016 (*Preprint* 1603.00501)
- [23] Sekiguchi Y, Kiuchi K, Kyutoku K, Shibata M and Taniguchi K 2016 *Phys. Rev.* **D93** 124046 (*Preprint* 1603.01918)
- [24] Dietrich T, Ujevic M, Tichy W, Bernuzzi S and Bruegmann B 2016 (*Preprint* 1607.06636)
- [25] Metzger B D 2016 (*Preprint* 1610.09381)
- [26] Read J S, Markakis C, Shibata M, Uryu K, Creighton J D *et al.* 2009 *Phys.Rev.* **D79** 124033 (*Preprint* 0901.3258)
- [27] Foucart F 2012 *Phys. Rev.* **D86** 124007 (*Preprint* 1207.6304)
- [28] Kawaguchi K, Kyutoku K, Shibata M and Tanaka M 2016 *Astrophys. J.* **825** 52 (*Preprint* 1601.07711)
- [29] Yagi K and Yunes N 2016 (*Preprint* 1608.02582)
- [30] Rosswog S 2015 *Int.J.Mod.Phys.* **D24** 1530012 (*Preprint* 1501.02081)
- [31] Radice D, Galeazzi F, Lippuner J, Roberts L F, Ott C D and Rezzolla L 2016 *Mon. Not. Roy. Astron. Soc.* **460** 3255–3271 (*Preprint* 1601.02426)

- [32] Palenzuela C, Liebling S L, Neilsen D, Lehner L, Caballero O L, O'Connor E and Anderson M 2015 *Phys. Rev. D* **92** 044045 (*Preprint* 1505.01607)
- [33] Dietrich T, Bernuzzi S, Ujevic M and Tichy W 2016 (*Preprint* 1611.07367)
- [34] Li L X and Paczynski B 1998 *Astrophys.J.* **507** L59 (*Preprint* astro-ph/9807272)
- [35] Metzger B, Martinez-Pinedo G, Darbha S, Quataert E, Arcones A *et al.* 2010 *Mon.Not.Roy.Astron.Soc.* **406** 2650 (*Preprint* 1001.5029)
- [36] Roberts L F, Kasen D, Lee W H and Ramirez-Ruiz E 2011 *Astrophys.J.* **736** L21 (*Preprint* 1104.5504)
- [37] Korobkin O, Rosswog S, Arcones A and Winteler C 2012 (*Preprint* 1206.2379)
- [38] Tanaka M 2016 *Adv. Astron.* **2016** 6341974 (*Preprint* 1605.07235)
- [39] Rosswog S, Feindt U, Korobkin O, Wu M R, Sollerman J, Goobar A and Martinez-Pinedo G 2016 (*Preprint* 1611.09822)
- [40] Fernandez R and Metzger B D 2016 *Ann. Rev. Nucl. Part. Sci.* **66** 2115 (*Preprint* 1512.05435)
- [41] Kasen D, Badnell N R and Barnes J 2013 *Astrophys. J.* **774** 25 (*Preprint* 1303.5788)
- [42] Wanajo S, Sekiguchi Y, Nishimura N, Kiuchi K, Kyutoku K and Shibata M 2014 *Astrophys. J.* **789** L39 (*Preprint* 1402.7317)
- [43] Tanaka M, Hotokezaka K, Kyutoku K, Wanajo S, Kiuchi K, Sekiguchi Y and Shibata M 2014 *Astrophys. J.* **780** 31 (*Preprint* 1310.2774)
- [44] Webpage Tanaka URL http://th.nao.ac.jp/MEMBER/tanaka/nr_merger_lightcurve.html
- [45] Webpage Karaguchi URL http://www2.yukawa.kyoto-u.ac.jp/~kyohei.kawaguchi/kn_calc/main.html
- [46] Abbott B P *et al.* (InterPlanetary Network, DES, INTEGRAL, La Silla-QUEST Survey, MWA, Fermi-LAT, J-GEM, DEC, GRAWITA, Pi of the Sky, Fermi GBM, MASTER, Swift, iPTF, VISTA, ASKAP, SkyMapper, PESSTO, TOROS, Pan-STARRS, Virgo, Liverpool Telescope, BOOTES, LIGO Scientific, LOFAR, C2PU, MAXI) 2016 *Astrophys. J.* **826** L13 (*Preprint* 1602.08492)